Contrast-Independent Curvilinear Structure Detection in Biomedical Images

Boguslaw Obara, *Member, IEEE*, Mark Fricker, David Gavaghan, and Vicente Grau, *Member, IEEE*

***Abstract*—Many biomedical applications require detection of curvilinear structures in images and would benefit from automatic or semiautomatic segmentation to allow high-throughput measurements. Here, we propose a contrast-independent approach to identify curvilinear structures based on oriented phase congruency, i.e., the phase congruency tensor (PCT). We show that the proposed method is largely insensitive to intensity variations along the curve and provides successful detection within noisy regions. The performance of the PCT is evaluated by comparing it with state-of-the-art intensity-based approaches on both synthetic and real biological images.**

***Index Terms*—Bioimage informatics, curvilinear structure, live-wire tracing, phase congruency tensor (PCT).**

I. Introduction

BIOMEDICAL image analysis plays a critical role in life sciences and health care [1]–[3]. In particular, robust and efficient enhancement, segmentation, analysis, and modeling of curve-like structures is a very common requirement in bioimage informatics. Therefore, a number of image processing solutions have been proposed to extract curvilinear structures including blood vessels [4], [5], airways in lung images [6], neurons [7], [8], dendritic spines [9], [10], microtubules [11]–[13], milk ducts, fibrous tissue [14], spiculations [15], [16], and many other similar entities [17].

This paper is organized as follows. The discussion of the most common image processing methods for the detection and the tracking of curvilinear objects is presented in Section I-A–F. The phase congruency tensor (PCT), which is a novel contrast-independent concept for curvilinear feature detection, is introduced in Section II. Section III compares the proposed approach with state-of-the-art intensity-based approaches, both on synthetic images (see Section III-A) and on images of saprotrophic fungi (see Section III-B). Section IV is dedicated to discussion and future work.

Manuscript received September 30, 2010; revised August 13, 2011; accepted January 12, 2012. Date of publication January 27, 2012; date of current version April 18, 2012. This work was supported by academic Grants from the Biotechnology and Biological Sciences Research Council and Engineering and Physical Sciences Research Council, U.K. The work of V. Grau is supported by Research Councils U.K. Academic Fellowship. The associate editor coordinating the review of this manuscript and approving it for publication was Prof. David S. Taubman.

B. Obara is with the Oxford e-Research Centre and Oxford Centre for Integrative Systems Biology, OX1 3QG Oxford, U.K. (e-mail: boguslaw.obara@oerc.ox.ac.uk).

M. Fricker is with the Department of Plant Sciences, University of Oxford, OX1 3RB Oxford, U.K. (e-mail: mark.fricker@plants.ox.ac.uk).

D. Gavaghan is with the Department of Computer Science, Oxford Centre for Integrative Systems Biology, OX1 3QU Oxford, U.K. (e-mail: david.gavaghan@comlab.ox.ac.uk).

V. Grau is with the Oxford e-Research Centre and Institute of Biomedical Engineering, Department of Engineering Science, University of Oxford, OX1 3QG Oxford, U.K. (e-mail: vicente.grau@eng.ox.ac.uk).

Color versions of one or more of the figures in this paper are available online at http://ieeexplore.ieee.org.

Digital Object Identifier 10.1109/TIP.2012.2185938

A. Matched Filters

Matched filters have been widely used to enhance and detect curvilinear objects observed in bioimages. The basic idea behind these filters is to locate the positions of objects represented by the ridges and the ravines in the image intensity function. Therefore, the shape of the matched filter is based on the spatial properties of the object to be recognized. In order to preserve rotation invariance, the filter is often rotated to a reasonable set of possible object orientations, and the maximum response from the filter bank is calculated. For instance, Chaudhuri *et al.* [4] have proposed an oriented Gaussian-shaped curve matching filter. The matched filter parameters can be estimated empirically or via an optimization process [18]. Based on this filter, an amplitude-modified second derivative of the Gaussian filter was introduced in [19]. Given the suitability of second-order derivative filters to detect curvilinear structures (which form either ridges or valleys when traversed across the structure), filters based on the second derivative of a Gaussian have been commonly used in linear structure detection, often through the calculation of the local Hessian matrix (see Section I-C).

Freeman and Adelson [20] proposed the concept of steerable filters, in which an oriented filter is constructed from a linear combination of a fixed set of directional derivatives of the Gaussian function. A spherically separable version of such filters for the detection of vascular structures has been recently presented in [21].

B. Using Tensors for Local Feature Characterization

In general, a tensor representation of an image can give information about how much the image varies along and across the dominant orientations within a certain neighborhood [22], [23]. A common approach to represent local image structure through a tensor is to consider the first terms of the Taylor series expansion [24], [25]. In the Taylor series, the second-order derivatives are incorporated in the Hessian matrix (a second-order tensor), which has been thus proposed to describe local shape orientation for elongated structures [26], [27]. More generally, a tensor representation of local orientation can be produced by combining the outputs from polar separable quadrature filters. Let us consider image $I(\mathbf{p})$, where $\mathbf{p} = [x, y]^T$ is a column vector representation of the spatial location. A suitable representation of the local shape of the surface in the neighborhood of $\mathbf{p}$ is given by the tensor defined as follows [22]:

$$T = \sum_o \|q_o\| \left(\mathbf{n}_o \mathbf{n}_o^T - \alpha \mathbb{I}\right) \quad (1)$$

where q_o is the output from an oriented quadrature filter in the direction specified by o, $\mathbf{n}_o$ is the normalized column vector in orientation o, $\alpha = 1/m - 1$, with m being the dimensionality of I, and $\mathbb{I}$ is the identity tensor. In the 2-D case, orientation o can be specified by a single angle $\theta(o)$, and $\mathbf{n}_\theta$ is the column vector given by

$$\mathbf{n}_\theta = [\cos(\theta), \sin(\theta)]^T. \tag{2}$$

C. Scale Space

Since curvilinear structures observed in the image can appear in different sizes, a scale space representation of an image has been extensively used [5], [26]–[30]. The basic idea is to embed the original image into a family of gradually smoothed images, in which the fine scale details are successively suppressed. This is commonly achieved through the use of Gaussian filters or their derivatives, with multiple scales achieved by varying the value of the variance. In the following, we assume a linear (Gaussian) scale space, but alternatives using nonlinear filters have been also proposed.

D. Hessian

For a given image $I(\mathbf{p})$ and a given scale σ, the neighborhood of point $\mathbf{p}$ can be approximated by its Taylor expansion, i.e.,

$$I_\sigma(\mathbf{p} + \Delta\mathbf{p}) \approx I_\sigma(\mathbf{p}) + \Delta\mathbf{p}^T \nabla I_\sigma(\mathbf{p}) + \Delta\mathbf{p}^T H_\sigma(\mathbf{p}) \Delta\mathbf{p} \tag{3}$$

where I_σ is the image representation at the given scale, defined by the convolution with a Gaussian kernel with variance σ. The Hessian matrix $H_\sigma(\mathbf{p})$ is the tensor of second partial derivatives of image I at scale σ and point $\mathbf{p}$.

By performing an eigenanalysis of the tensor representing the local structure, we can calculate the principal orientations (the normalized eigenvectors of tensor $\mathbf{u}_{\sigma,i}$) and the output of the feature detector in these orientations (eigenvalues $\lambda_{\sigma,i}$, satisfying $|\lambda_{\sigma,i}| \leq |\lambda_{\sigma,i+1}|$).

In three dimensions, a spherical neighborhood centered at point $\mathbf{p}$ is mapped by $H_\sigma(\mathbf{p})$ onto an ellipsoid whose axes are along the directions given by eigenvectors $\mathbf{u}_{\sigma,i}$ of the Hessian and the corresponding axis' semilengths are the magnitudes of the respective eigenvalues $\lambda_{\sigma,i}$. Hence, the detection of piecewise curvilinear segments can be done by an analysis of the eigenvectors and the eigenvalues (their absolute values and the relations between them). Two of the ways in which this has been tackled in the literature, namely, vesselness and neuriteness, are explained in the following sections.

Vesselness: For a given scale σ, the Hessian matrix of the image is computed, and the following measure [5] is calculated (this corresponds to the 2-D case, but it can be easily extended to n dimensions), i.e.,

$$V_\sigma = e^{-\frac{\lambda_{\sigma,1}^2}{2\beta^2\lambda_{\sigma,2}^2}} \left(1 - e^{-\frac{\lambda_{\sigma,1}^2 + \lambda_{\sigma,2}^2}{2c^2}}\right) \tag{4}$$

where $\lambda_{\sigma,1}$ and $\lambda_{\sigma,2}$ are the eigenvalues of $H_\sigma(\mathbf{p})$, and β and c are thresholds that control the sensitivity of the line measurement. The first exponential in (4) depends on the ratio between the first and second eigenvalues, and is thus minimized for blob-like structures and increases as the disparity between the parallel and orthogonal curvature values increases, whereas the second component is responsible for a measure of the relative brightness/darkness of the curvilinear structure and is used to differentiate noise from well-defined structures. Multiscale vesselness, for a given set of scales Σ, is computed as follows:

$$V_\Sigma = \max_{\sigma \in \Sigma}(V_\sigma). \tag{5}$$

Neuriteness: For a given scale σ, an alternative measurement of piecewise linear segments that is also based on the Hessian matrix was proposed in [7], i.e.,

$$N_\sigma = \begin{cases} \frac{\lambda_\sigma}{\lambda_{\sigma,\min}}, & \text{if } \lambda_\sigma < 0 \\ 0, & \text{if } \lambda_\sigma \geq 0 \end{cases} \tag{6}$$

where

$$\lambda'_{\sigma,1} = \lambda_{\sigma,1} + \alpha\lambda_{\sigma,2} \tag{7}$$

$$\lambda'_{\sigma,2} = \lambda_{\sigma,2} + \alpha\lambda_{\sigma,1} \tag{8}$$

$$\lambda_\sigma = \max\left(\left|\lambda'_{\sigma,1}\right|, \left|\lambda'_{\sigma,2}\right|\right) \tag{9}$$

$$\lambda_{\sigma,\min} = \min_{\mathbf{p} \in I}(\lambda_\sigma). \tag{10}$$

where $\lambda_{\sigma,1}$ and $\lambda_{\sigma,2}$ are the eigenvalues of the Hessian matrix $H_\sigma(\mathbf{p})$ for a given scale parameter σ. Parameter α is chosen such that the equivalent steerable filter [20] used in the calculation of the Hessian matrix is maximally flat in its longitudinal direction.

E. Phase-Based Detection

In the search for contrast-independent curvilinear feature detection in images, image processing approaches based on local image phase rather than image intensity have been explored. The computation of local phase requires the application of quadrature pairs of filters to the image. Thus, for a given image $I(\mathbf{p})$ and a quadrature pair of even and odd filters $F_{\text{so}}^{\text{even}}$ and $F_{\text{so}}^{\text{odd}}$ at scale s and orientation o, the response vector is given by its even and odd components $e_{\text{so}}(\mathbf{p})$ and $d_{\text{so}}(\mathbf{p})$, i.e.,

$$[e_{\text{so}}(\mathbf{p}), d_{\text{so}}(\mathbf{p})] = \left[I(\mathbf{p}) * F_{\text{so}}^{\text{even}}, I(\mathbf{p}) * F_{\text{so}}^{\text{odd}}\right]. \tag{11}$$

The amplitude of the soth component is defined as

$$A_{\text{so}}(\mathbf{p}) = \sqrt{e_{\text{so}}(\mathbf{p})^2 + d_{\text{so}}(\mathbf{p})^2} \tag{12}$$

and the local phase is given by

$$\phi_{\text{so}}(\mathbf{p}) = \text{atan}\left(\frac{d_{\text{so}}(\mathbf{p})}{e_{\text{so}}(\mathbf{p})}\right). \tag{13}$$

A number of quadrature filters have been proposed for phase detection in images. Below, we discuss the log-Gabor filter (one of the most common and the one we are using in this paper); a more a comprehensive review of quadrature filters can be found in [31].

Log-Gabor Filter: Gabor-based filters, first proposed by Gabor [32] are a traditional choice for quadrature filters. The log-Gabor filter, proposed in [33], is basically a logarithmic transformation of the Gabor filter, which eliminates the zero frequency component. The log-Gabor filter has an extended tail at the high-frequency end, similar to the amplitude spectra of natural images [31]. In 2-D, the oriented log-Gabor filter in the

frequency domain can be defined in polar coordinates as the product of two components, which are radial, i.e.,

$$\hat{\mathcal{H}}(\omega) = e^{-\frac{\left(\log\left(\frac{\omega}{\omega_0}\right)\right)^2}{2\left(\log\left(\frac{\sigma_\omega}{\omega_0}\right)\right)}} \tag{14}$$

and angular, i.e.,

$$\hat{\mathcal{H}}(\theta) = e^{-\frac{(\theta-\theta_0)^2}{2\sigma_\theta}} \tag{15}$$

where ω_0 is the center frequency of the filter, σ_ω controls the frequency spread of the filter, θ_0 is the orientation of the filter, and σ_θ determines the angular spread.

Phase Congruency: Methods based on phase have been proposed as a contrast-invariant alternative to more widespread intensity-based ones. In particular, the concept of phase congruency has been used to find a wide range of feature types including step edges, line and roof edges, and Mach bands. The phase congruency model postulates that features are perceived at points where the Fourier components are maximally in phase [34]–[36].

Different practical ways to calculate phase congruency have been proposed [34], [35], [37], [38]. A robust approach was introduced in [38], combining information over several scales and orientations and including a noise compensation term (since phase congruency is contrast independent, it can be sensitive to noise). Alternatively, the information about the way phase congruency varies with orientation can be represented by combining phase congruency information over multiple orientations into a covariance matrix and calculating the minimum and maximum moments [39].

In [38], 2-D phase congruency is calculated as the sum of phase congruencies at several orientations, i.e.,

$$\mathrm{PC}(\mathbf{p}) = \sum_o \mathrm{PC}_o(\mathbf{p}) \tag{16}$$

where the phase congruency at each orientation o is defined as

$$\mathrm{PC}_o(\mathbf{p}) = \frac{\sum_s W(\mathbf{p})\left[A_{\mathrm{so}}(\mathbf{p})\Delta\mathbf{\Phi}_{\mathrm{so}}(\mathbf{p}) - t\right]}{\sum_s A_{\mathrm{so}}(\mathbf{p}) + \epsilon} \tag{17}$$

where $A_{\mathrm{so}}(\mathbf{p})$ is the amplitude of the image component at scale s and orientation o, as defined in (12), t is a noise threshold, ϵ is a small real number used to avoid division by zero, and the brackets [] represent the operation by which values smaller than zero are set to zero. $\Delta\mathbf{\Phi}_{\mathrm{so}}(\mathbf{p})$ is a phase deviation measure, quantifying the difference between phase at scale s and orientation o, $\phi_{\mathrm{so}}(\mathbf{p})$, and the mean phase angle at orientation o, $\bar{\phi}_o$, calculated as follows:

$$\Delta\mathbf{\Phi}_{\mathrm{so}}(\mathbf{p}) = \cos\left(\phi_{\mathrm{so}}(\mathbf{p}) - \bar{\phi}_o(\mathbf{p})\right) - \left|\sin\left(\phi_{\mathrm{so}}(\mathbf{p}) - \bar{\phi}_o(\mathbf{p})\right)\right| \tag{18}$$

$W(\mathbf{p})$ is a sigmoid-based weighting function that reduces phase congruency at locations with a narrow frequency component, defined as follows:

$$W(\mathbf{p}) = \left(1 + e^{\gamma\left(c - \frac{1}{S}\left(\frac{\sum_s A_s(\mathbf{p})}{A_{\max}(\mathbf{p})+\epsilon}\right)\right)}\right)^{-1} \tag{19}$$

with S being the total number of scales, $A_{\max}$ being the maximum of the scale responses, and c and γ defining the shape of the sigmoid (c is the "cutoff" value below which phase congruency values are penalized, and γ is a gain factor that controls the sharpness of the "cutoff").

An alternative approach for the calculation of the phase is the monogenic signal, which is an extension of the analytic signal using the Riesz transform that was proposed in [36]. Different from this, our approach is based on the calculation of phase values in several orientations to characterize local n-dimensional structure, and thus, we rely on the approach from [38], which has been widely used and provides additional noise reduction. A related approach, developed in parallel with this paper, was presented in [40]. This approach is based on phase congruency and tensor voting, and makes use of the properties of how the primary visual cortex responds to edges and lines built from the Fourier decomposition of an image.

F. Tracing

After the application of a feature detection filter, a subsequent step is required to identify the curvilinear structures. This can be as simple as applying a threshold, but to ensure connectivity and improve performance in the presence of noise, a number of tracing (or tracking) methods have been proposed. In general, tracing methods for biomedical imaging applications use a model to follow the curvilinear structures, starting at given points [41]. Tracing methods often tend to terminate at branch points, from which each branch can be then separately processed [8]. The starting points are often manually placed or found by using local thresholding techniques. For instance, Can *et al.* [42] proposed the combination of 2-D correlation kernels perpendicular to the direction of the curvilinear objects and low-pass averaging filters along them. A tracing approach based on hidden Markov models was explored in [13]. In [43], separate templates were constructed for the left and right boundaries of the traced structures, along different orientations.

An interesting approach relies on the use of minimum cost paths [44], an example of which is the live-wire algorithm [45]. In the live-wire method, the minimum cost path is calculated on a graph representation of the image and using Dijkstra shortest-path algorithm [44]. The shortest path is defined as a path from one node/pixel to another such that the sum of the costs of the arcs on the path is minimized. The use of minimum cost path algorithms and window-constrained global search was suggested in [46]. In [47], an approach that combines directional matched filtering with an algorithm for finding minimum cost paths was proposed.

The method proposed in this paper is closely related to that in [7], which proposed a semiautomatic approach to trace 2-D curvilinear structures that uses local principal ridge directions to guide the live-wire algorithm along centerlines.

The cost of the path from pixel $\mathbf{p}$ to an eight-connected neighboring pixel $\mathbf{r}$ is computed using the following formula [7]:

$$C(\mathbf{p},\mathbf{r}) = \gamma C_i(\mathbf{r}) + (1-\gamma)C_v(\mathbf{p},\mathbf{r}) \tag{20}$$

where C_i is a normalized image intensity based cost and C_v is a vector-field-based cost, which is calculated as follows:

$$C_v(\mathbf{p},\mathbf{r}) = \frac{1}{2}\left\{\sqrt{1 - \|\phi(\mathbf{p},\mathbf{r})\|} + \sqrt{1 - \|\phi(\mathbf{r},\mathbf{p})\|}\right\} \tag{21}$$

$$\phi(\mathbf{p},\mathbf{r}) = |V(\mathbf{p}) \cdot \mathbf{d}(\mathbf{p},\mathbf{r})| \tag{22}$$

$$\mathbf{d}(\mathbf{p},\mathbf{r}) = (\mathbf{r}-\mathbf{p})/\|\mathbf{r}-\mathbf{p}\| \tag{23}$$

where $V(\mathbf{p})$ is the value of the vector field at point $\mathbf{p}$. The value of $\gamma \in [0,1]$ determines the relative weight of the C_i and C_v cost components. These two components are independently calculated, and the issue of scaling between them needs to be addressed. In our case, this is done by normalizing both of them to the [0, 1] range. Still, the selection of value γ needs to be carefully considered.

G. Contributions of This Paper

In this paper, we propose a new phase-based concept for curvilinear feature detection, called the PCT. This method expands the idea of phase congruency to incorporate the local structure of the image at different orientations, thus keeping the contrast-invariant property of phase-based methods while allowing the detection of structures with specific shapes. We apply this concept to the detection of curvilinear structures, in a way similar to the vesselness and neuriteness calculations previously explained, which results in the definition of PCT-based vesselness and PCT-based neuriteness. We demonstrate the PCT-based methods and compare them with standard approaches, both on their own as feature detection tools and in combination with a minimal cost tracing algorithm. Finally, we demonstrate the use of the PCT-based live-wire tracing approach in a challenging biomedical image processing application, i.e., the characterization of fungal network images.

II. Method

A. PCT

The detection of curvilinear structures is particularly affected by variations of intensity contrast within the image. Intensity differences between curvilinear structures and with the background, common to many biomedical imaging applications, cause traditional intensity-based methods to produce widely varying outputs, which, in turn, make it difficult for postprocessing methods to delineate the structures. Additionally, the boundaries of low-contrast structures may not be detected by methods based on the image gradient. Therefore, it is essential that the approach is invariant to changes in image intensity and contrast. Changes in intensity may occur because of varying illumination, signal variations, bias fields in magnetic resonance imaging, etc.

Here, we propose a brightness- and contrast-invariant method for curvilinear structure extraction based on the concept of local phase and particularly on a model of phase congruency, which assumes that image features are observed at points in an image where the Fourier components are maximally in phase. Phase-based ridge detectors, such as [16], have been shown to be able to detect such structures in a largely contrast-independent way. The difference between the phase-based ridge detectors and our approach is given by the relation between outputs at different orientations. We propose to combine all values of orientation-specific phase congruency in a single tensor, the eigenanalysis of which can be used as a contrast-independent description of the local structure.

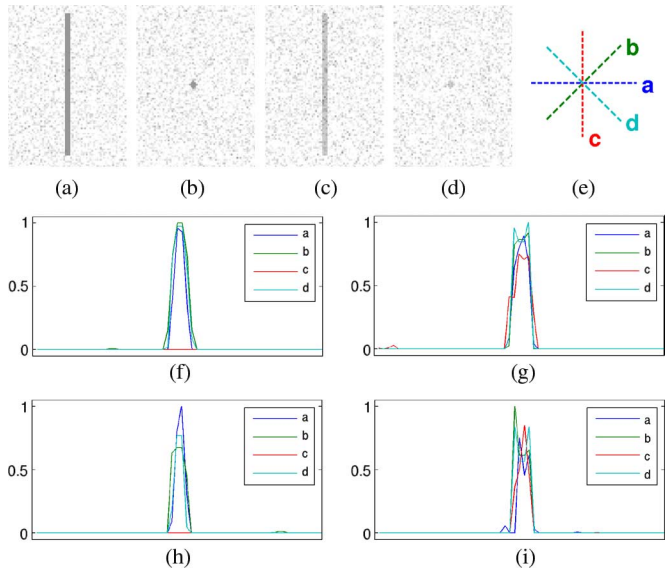

Fig. 1. PCT concept. Synthetic image of (a, b) high and (c, d) low contrast line and blob with Gaussian white noise of zero mean and 0.2 variance applied. (e) Lines represent directions for which the phase congruency and PCT are calculated. (f, g, h, i) Profile represents values of PC_o calculated, along the lines defined in Fig. 1(e), for images in Fig. 1(a)–(d), respectively. Corresponding PC values at the point of intersection of the profile lines are 0.85, 0.90, 0.8, and 0.85 for images in Fig. 1(a)–(d), respectively, illustrating that PC on its own does not differentiate lines from blobs.

To illustrate our concept, Fig. 1 shows low- and high-contrast linelike and bloblike objects in a noisy background. The phase congruency measures in selected orientations [see Fig. 1(e)], i.e., PC_o, as defined in (17), are calculated and presented in Fig. 1(f)–(i). As expected, the values of PC_o are barely affected by the contrast changes, but more importantly, a high value of phase congruency PC_o is obtained in the direction perpendicular to the linear structure, while the values in the direction parallel to the structure remain close to zero. This is in contrast to bloblike structures, where PC_o values remain high for all orientations [see red line plot in Fig. 1(f)–(i)]. The difference between lines and blobs is however suppressed in the phase congruency measure PC, which combines all orientation-specific phase congruencies PC_o; PC values are 0.85–0.8 for lines and 0.9–0.85 for blobs. Therefore, the phase congruency measure PC does not provide on its own a suitable way of expressing this behavior, and the relationship between PC_o measures has to be used.

We thus propose to exploit this idea to define a contrast-independent tensor-based approach to quantify the local behavior of the image intensity function, i.e., the PCT. For a given set of scales $\{s\}$ and a given set of phase congruency measures $\mathrm{PC}_o(\mathbf{p})$ (for each orientation o), analogous to (1), we propose the PCT to take the following form:

$$T_{\mathrm{PC}} = \sum_o \mathrm{PC}_o(\mathbf{p}) \left(\mathbf{n}_o \mathbf{n}_o^T - \alpha \mathbb{I}\right). \tag{24}$$

Through the use of its eigenvalues and eigenvectors, the PCT can be used to reduce contrast dependence in many other approaches for the detection and the analysis of curvilinear structures observed in biomedical images. Its use in exchange for the Hessian matrix in vesselness [5], [26], [27] and neuriteness [7]

is illustrated in the following sections, as well as its introduction within a live-wire tracing method [7], [48]. Other possibilities such as its use in anisotropic diffusion schemes have be also explored [49].

B. PCT Vesselness and Neuriteness

As described in Section I-D1 and I-D2, piecewise curvilinear segments can be detected by analyzing the relations between eigenvalues and eigenvectors of the locally calculated Hessian. In a similar way, the dominant orientation of the surface representing a curvilinear structure is given by the dominant eigenvector of T_{PC}, i.e., the eigenvector corresponding to the eigenvalue of largest magnitude. PCT-based vesselness and neuriteness are calculated using (4) and (6), where the eigenvalues of T_{PC} substitute those of the Hessian.

C. PCT Live-Wire Tracing

In order to apply the live-wire tracing method discussed in Section I-F, the eight-connected graph representation of the image is constructed. Then, the cost map combining the image intensity cost C_i and the vector-field cost C_v is calculated as defined in (20)–(23). We study the use of different cost functions based on previously available intensity-based techniques and our proposed PCT.

For the vesselness-based tracing, the C_i component of the cost map corresponds to the vesselness measurement V_Σ as defined in (5). In order to take full advantage of both intensity- and orientation-based cost map components, we also introduce the C_v component based on the vesselness measurement. The vector-field-based C_v is defined by eigenvectors corresponding to V_Σ, which are obtained using the following formula:

$$\sigma_{\max} = \arg\max_{\sigma\in\Sigma}(V_\sigma) \tag{25}$$

$$\mathbf{u}_{\Sigma,i} = \mathbf{u}_{\sigma_{\max},i} \tag{26}$$

where $\sigma_{\max}$ represents the scale for which the maximum vesselness occurs. Eigenvectors $\mathbf{u}_{\Sigma,i}$ correspond to eigenvalues $\lambda_{\Sigma,i}$, which were used to define the multiscale vesselness V_Σ. The new vesselness measure including the vector-field component will be called "VF vesselness."

We also investigate the behavior of neuriteness-based live-wire tracing, in which case C_i corresponds to N_σ as defined in (6) and C_v is based on the eigenvectors of the Hessian matrix as defined in (7)–(10).

The cost maps C_i for PCT vesselness and neuriteness are calculated using (4) and (6), where the eigenvalues of T_{PC} are used. In the same way, the corresponding C_v value are calculated using the eigenvectors of T_{PC}.

III. Results

A. Synthetic Images

We tested the performance of the PCT-based method for curvilinear structure detection on synthetic images and real biological images (see Section III-B). A synthetic image [see Fig. 2(a)] was designed to simulate branching structures in a noisy environment. Grid lines with a width of 10 pixels were generated on a bright constant background. To simulate real-life noise, a fog filter plugin for the widely used image processing program GIMP was used [50].

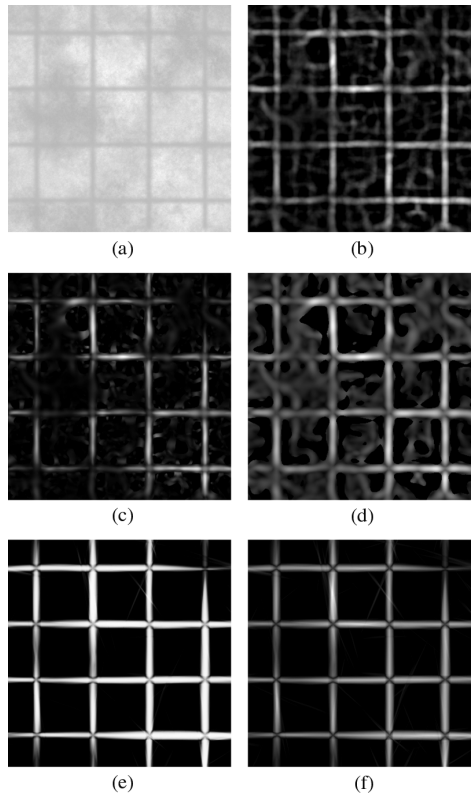

Fig. 2. Comparison between feature detection methods on synthetic images after noise is added. (a) Original synthetic image showing branching patterns. (b–f) Results using intensity-based methods and our PCT-based approach, namely, (b) Gaussian, (c) vesselness, (d) neuriteness, (e) PCT vesselness, and (f) PCT neuriteness.

For comparison, we calculated the outputs of relevant previously available methods including a Gaussian matched filter (as defined by [4]; we will refer to it as Gaussian in the following), vesselness [as defined in (5)], and neuriteness [as defined in (6)]. The results of these and the PCT vesselness and neuriteness are presented in Fig. 2(b)–(f). The parameters used in these tests were manually optimized to provide the best visual detection, with the PCT-based parameters kept exactly the same as those for their respective intensity-based measures. For reproducibility, we present a full list of parameters.

1) Gaussian: $\sigma = 3$, $\theta = k\pi/6$, $\forall k \in [0, 1, 2, 3, 4, 5]$;
2) Vesselness/PCT vesselness: $\Sigma = \{2 + (k/2)\}$, $\forall\ k \in [0, 1, 2, 3, 4]$, $\gamma = 2$, and $\beta = 0.5$ $c = 15$;
3) Neuriteness/PCT neuriteness: $\sigma = 3$;
4) Phase congruency: $\omega_0 = 1/(5.4)^{s-1}$, $\forall s \in [1, 2, 3, 4]$, $\sigma_\omega/\omega_0 = 1.2$, $c = 0.4$, $\gamma = 10$, and t is calculated using the median to estimate noise level, as described in [38].

For the functions containing two terms, as in (20), the value of $gamma$ was set to 0.5; thus, the maximum contribution is the same in both terms. Changes around this value appeared to have a limited effect in the results. For definitions, see Section I-F.

B. Application to Fungal Network Extraction

We have applied the proposed approach in a challenging bioimaging application, using a live-wire tracing method, based

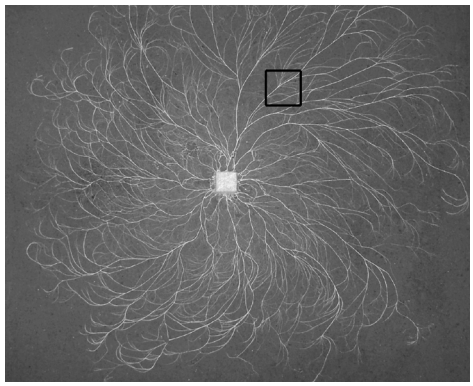

Fig. 3. Image of a fungal network acquired using a digital camera. The square delimits the region of interest that we have used to illustrate the performance of the methods in Figs. 4 and 5.

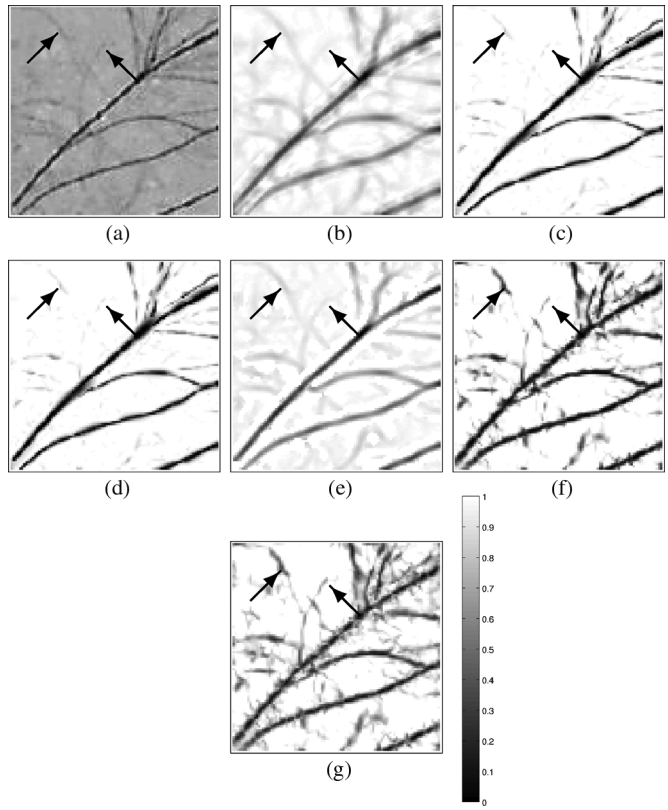

Fig. 4. Comparison of cost maps for the live-wire algorithm, obtained using different algorithms and only the intensity cost term ($\gamma = 1$): (a) Original image, (b) Gaussian, (c) vesselness, (d) VF vesselness, (e) neuriteness, (f) PCT vesselness, and (g) PCT neuriteness. (Arrows) Low-contrast branches where the intensity-based algorithms fail. As it can be noticed, the images in (c) and (d) are exactly the same (they are both based only on the intensity term, kept here for consistency with Fig. 5).

on the description in Section I-F, to extract branches in images of saprotrophic fungal networks.

Fungal Networks: Saprotrophic fungi are critical in ecosystem biology as they are the only organisms capable of complete degradation of wood in temperate forests. These fungi form extensive interconnected mycelial networks that efficiently scavenge for scarce resources in a heterogeneous environment (see Fig. 3). This network is formed from the aggregation of individual hyphae termed cords. The architecture of the network continuously adapts to local nutritional cues, damage, or predation, through growth, branching, fusion, or regression [51]. These networks also provide an example of an experimental planar network system that can be subjected to both theoretical analysis and experimental manipulation in multiple replicates. For high-throughput measurements, we need to be able to automatically analyze the dynamic network architecture to evaluate their performance efficiently. With thousands of branches on each image, manual detection is not a viable option, particularly if temporal sequences are taken. Furthermore, branches typically show considerable variation in contrast not only because of the difficulty in achieving a homogeneous intensity against a varying background but also because the cords vary in size over two orders of magnitude. In these conditions, the automatic characterization of the fungal networks is challenging for conventional intensity-based approaches, and the manual analysis is still the state of the art [51].

Tracing Comparison: We applied a live-wire tracing algorithm for fungal network detection based on the cost maps calculated, as described in Sections I-F and II-C, and using different intensity-based, as well as our proposed PCT-based feature detection methods, to define the costs. The comparison of these cost maps, calculated for the region of interest outlined in Fig. 3, is presented in Figs. 4 (C_i component) and 5 (C_v component calculated for a line traced in the northeast direction of the graph).

After selecting the start point and the endpoint manually of a branch of interest, the shortest path is calculated between these, as presented in Fig. 6. This represents an interesting challenge for the live-wire algorithm as the branch to be traced initially runs relatively close to a much brighter main cord. Thus, most of the methods automatically trace the stronger cord and then "jump" across to the correct branch. This error is dramatically reduced using PCT-based methods, particularly as the contribution of the vector field is introduced (see Fig. 6). For clarity of the visual representation, we only show three traces on each image, i.e., one of the manual tracings and the results of vesselness and PCT vesselness. These are the representative of *ground truth* and the results obtained using intensity-based and PCT-based measurements, respectively.

To quantify the performance of the proposed approach, 40 complex regions of interest in fungal images were selected. Manual tracings of specific cords were performed by two experts, as *ground truth* (GT1 and GT2).

GT and estimated traces were compared using the trace body distance ϵ_d measure proposed in [52]. The trace distance error is defined as the average distance between each point on the GT trace and the corresponding closest point on the automatic trace. First, the evaluation of distance error measure between GT1 and GT2 traces obtained by the first and second experts was performed. Of the 40 regions, only one showed a clear disagreement between the two experts and was eliminated. The distance error between the 39 remaining GT1 and GT2 traces was $\epsilon_d = 0.35$ [pixel]. Finally, the distance error evaluation between GT1/GT2 traces and traces obtained by the proposed approach is presented in Table I. The first result, labeled as "Image," corresponds to the one obtained using the image intensity directly

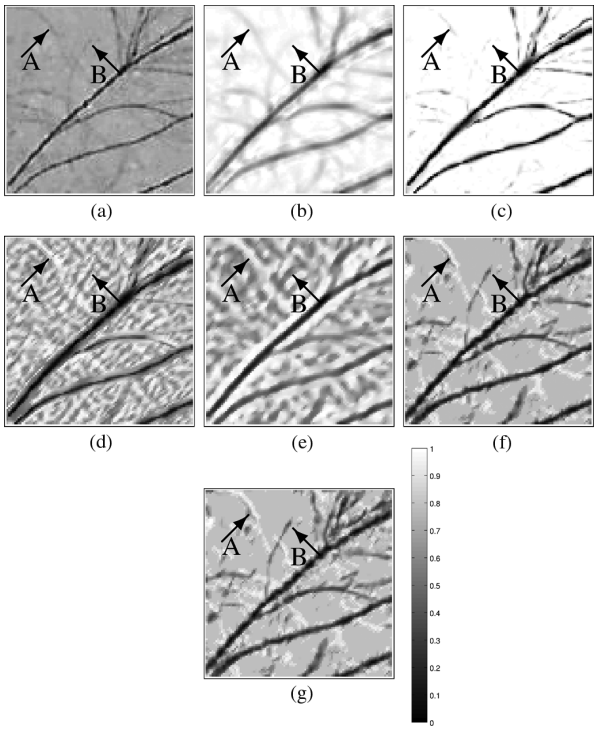

Fig. 5. Comparison of cost maps for the live-wire algorithm, obtained using different algorithms with a linear combination of intensity and direction cost terms ($\gamma = 0.5$). The images show the cost of tracing a line in the northeast (NE) direction: (a) Original image, (b) Gaussian, (c) vesselness, (d) VF vesselness, (e) neuriteness, (f) PCT vesselness, and (g) PCT neuriteness. (Arrows) Low contrast branches (A) across and (B) along the NE direction, where detection using intensity-based algorithms is challenged.

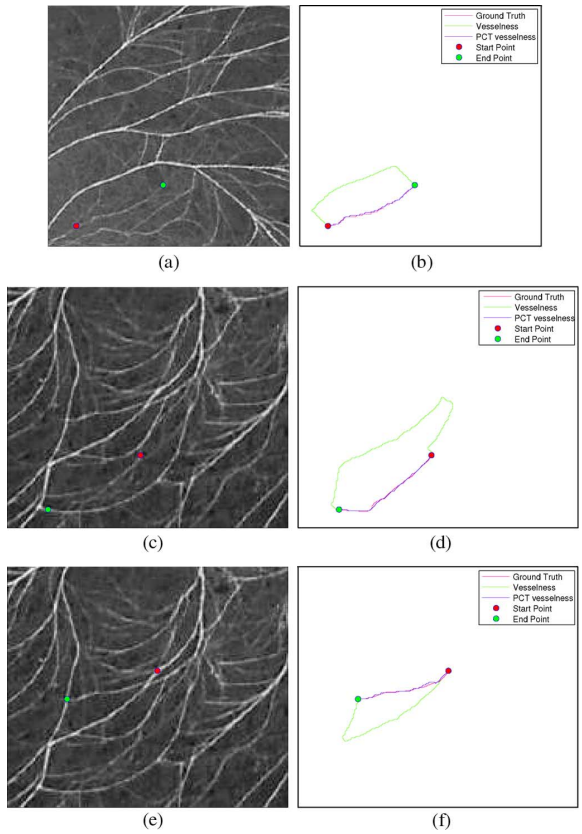

Fig. 6. Live-wire tracing comparison: (a, c, and e) Input image with the start point and the endpoint. (b, d, and f) *Ground truth* and obtained traces using $\gamma = 0.5$ (intensity + vector field).

as the intensity-based cost term. Those results where the algorithm was clearly not able to find a good approximation to the branch (defined as those with an error value larger than branch width) were labeled as "false" and not used in the calculation of the average distance. The number of false results is the same for the two experts (see Table I).

C. Other Applications

While our validation up to now has focused on fungal network extraction, the method proposed here shows considerable potential in many other applications. Fig. 7 shows sample results in the detection of the vessel tree in a retina and in a leaf. Further validation in other applications is the subject of future work.

D. Runtime Performance

The runtime performance of the implemented methods was tested on a personal computer with Intel Core 2 Duo (T8300) system with 2-GB memory, running Linux and MATLAB R2009b. Grayscale fungal network images of 100×100 pixels were used, and the average runtimes spent to calculate the cost function are presented in Table II.

TABLE I
TRACE DISTANCE ERROR AND NUMBER OF FALSE RESULTS USING EACH OF THE METHODS. FOR THOSE METHODS IN WHICH BOTH INTENSITY AND ORIENTATION COSTS WERE USED, A VALUE OF $\gamma = 0.5$ WAS USED

Method	GT1 - ϵ_d [pixel]	GT2 - ϵ_d [pixel]	False
image	1.29	1.35	24
Gaussian	1.16	1.21	24
vesselness	1.12	1.13	22
VF vesselness	1.17	1.15	18
neuriteness	1.15	1.70	13
PCT vesselness	0.78	0.85	2
PCT neuriteness	0.80	0.88	2

TABLE II
RUNTIME PERFORMANCE COMPARISON. A VALUE OF $\gamma = 0.5$ WAS USED

Method	Time [s]
image	0
Gaussian	0.05
vesselness	0.11
VF vesselness	2.52
neuriteness	2.47
PCT vesselness	2.60
PCT neuriteness	2.61

IV. DISCUSSION AND FUTURE WORK

In this paper, the concept of the PCT for curvilinear feature detection has been introduced (see Section II). An immediate use of the PCT is to substitute for other tensor representations, such as the Hessian, to strongly reduce the dependence on local image contrast. In particular, the PCT concept was used to define two curvilinear feature detection techniques, i.e., PCT vesselness and neuriteness, and was demonstrated in the context of a live-wire tracing method. In Section III-A, the PCT-based methods were compared with their corresponding

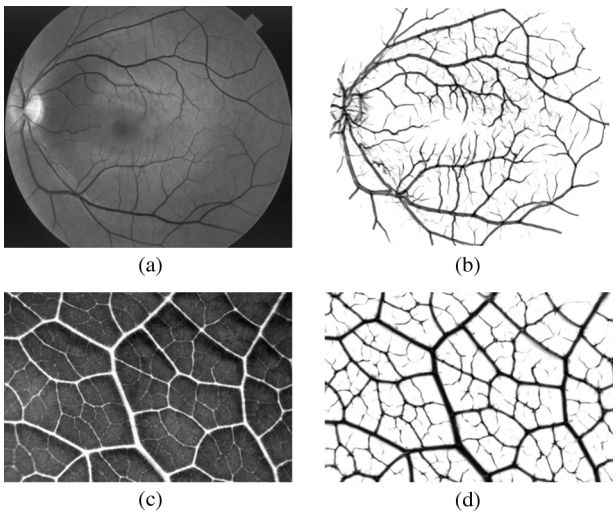

Fig. 7. Detection of curvilinear features observed on retina and leaf images: (a) Retina image "0255" from STARE database [53], (b) corresponding PCT vesselness measure, (c) leaf image, and (e) corresponding PCT vesselness measure.

intensity-based versions. The results shown in Fig. 2 illustrate the variations in the output for intensity-based methods when applied to structures with varying contrast. This complicates the choice of single thresholds for feature identification. In contrast, results presented for the PCT-based approaches show a much higher degree of uniformity in the results, which greatly facilitates postprocessing and accurate feature detection. It is apparent from the figures that PCT-based methods are the preferred option when structures with different contrasts are present. It is important to note that Hessian-based measurements, such as vesselness and neuriteness, are not valid at branching points and endpoints due to the ambiguity of the directions of the Hessian eigenvectors [21]. The PCT vesselness and neuriteness suffer from the same issues (see Fig. 2). The detection of branching points and endpoints is a related problem outside of the aims of this paper and is the subject of our work presented in [54]. The phase congruency can also be sensitive to noise. In this respect, the PC definition used here includes a noise reduction factor, which has an important effect in reducing noise. The use of several scales and orientations further reduces the noise effects.

To evaluate the performance of the new approach, we applied a PCT-based live-wire tracing method to detect fungal networks, and the results are presented in Section III-B. Fig. 4 shows the image intensity component of the cost maps, and Fig. 5 incorporates the vector-field component of the cost maps calculated in northeast direction of the graph. As shown, fungal branches along the northeast direction are detected (arrows B), and those across it are suppressed (arrows A). The visual inspection of the cost maps confirms the robustness of the PCT-based approaches against changes of the contrast of fungal structures and shows that the proposed method is capable of giving high detection responses even on low-contrast branches, pointed out by arrows in Figs. 4 and 5. Thereafter, we quantitatively compared the traces calculated based on standard and PCT-based cost maps with the *ground truth* trace, manually delineated by an expert. From Fig. 6, the improvement in the accuracy of the PCT-based methods is apparent. In the intensity-based methods, the presence of a higher intensity branch produces a path of lower cost compared with the branch of interest, and thus, the traces tend to lie on these high-intensity structures. By contrast, the PCT-based measure evens out the output from low- and high-contrast structures, making the detection of the correct branch much more likely. Finally, we performed a quantitative evaluation of the live-wire tracing of the fungal network with the results presented in Table I. The image and Gaussian cost map-based tracings give the highest number of false traces. The tracing is slightly better when the vesselness, the vesselness with the vector-field component, and the neuriteness are used for the cost calculation. The number of false results dramatically decreases (to 2 out of 40 cases) when the PCT-based methods are used. The overall distance to the *ground truth* is also smaller in the PCT-based methods, although the most difficult cases (those discarded as "false") were not taken into account in the intensity-based methods. Thus, the quantitative comparison confirms the improvement obtained when PCT-based methods are used for semiautomated fungal network detection. To summarize, the obtained results show that PCT-based methods are robust against changes of the intensity contrast of curvilinear structures and are capable of providing high detection responses on low-contrast edges. These properties are essential for detecting the structures in low-contrast regions of images, which can contain intensity inhomogeneity; these structures are common in a large number of biomedical images. In particular, images of the retina and the leaf have been used to demonstrate the versatility of the proposed approach in different domains (see Fig. 7). The runtime performance of PCT-based methods is very similar to their standard versions (the comparison is presented in Table II). The runtime values were obtained in a MATLAB implementation and might be susceptible to significant improvement if a low-level language version was developed. Finally, the PCT-based approach could be adapted to methods for finding other non-curvilinear structures such as junctions or ending points where high curvature values exist along more than one principal directions [55], [56]. The applicability of the PCT concept to junction detection has been shown in [54]. While the methods described in this paper have been applied to 2-D images, the definition of PCT is easily extendable to 3-D or higher dimensionality images.

REFERENCES

[1] A. Laine, "In the spotlight: Biomedical imaging," *IEEE Rev. Biomed. Eng.*, vol. 2, pp. 6–8, 2009.

[2] J. Swedlow, I. Goldberg, E. Brauner, and P. Sorger, "Informatics and quantitative analysis in biological imaging," *Science*, vol. 300, no. 5616, pp. 100–102, 2003.

[3] K. Kvilekval, D. Fedorov, B. Obara, A. K. Singh, and B. Manjunath, "Bisque: A platform for bioimage analysis and management," *Bioinformatics*, vol. 26, no. 4, pp. 544–552, Feb. 2010.

[4] S. Chaudhuri, S. Chatterjee, N. Katz, M. Nelson, and M. Goldbaum, "Detection of blood vessels in retinal images using two dimensional matched filters," *IEEE Trans. Med. Imag.*, vol. 8, no. 3, pp. 263–269, Sep. 1989.

[5] A. Frangi, W. Niessen, K. Vincken, and M. Viergever, "Multiscale vessel enhancement filtering," in *Proc. Med. Image Comput. Comput.-Assist. Interv.*, Oct. 11–13, 1998, vol. 1496, pp. 130–137.

[6] P. Lo, B. van Ginneken, J. Reinhardt, and M. de Bruijne, "Extraction of airways from CT," in *Proc. 2nd Int. Workshop Pulmonary Image Anal., Med. Image Comput. Comput.-Assist. Interv.*, Sep. 20–24, 2009, pp. 175–189.

[7] E. Meijering, M. Jacob, J. Sarria, P. Steiner, H. Hirling, and M. Unser, "Design and validation of a tool for neurite tracing and analysis in fluorescence microscopy images," *Cytometry A*, vol. 58, no. 2, pp. 167–176, Apr. 2004.

[8] G. Xiong, X. Zhou, A. Degterev, L. Ji, and S. Wong, "Automated neurite labeling and analysis in fluorescence microscopy images," *Cytometry A*, vol. 69, no. 6, pp. 494–505, Jun. 2006.

[9] Y. Zhang, X. Zhou, R. Witt, B. Sabatini, D. Adjeroh, and S. Wong, "Dendritic spine detection using curvilinear structure detector and LDA classifier," *NeuroImage*, vol. 36, no. 2, pp. 346–360, Jun. 2007.

[10] A. Rodriguez, D. Ehlenberger, D. Dickstein, P. Hof, and S. Wearne, "Automated three-dimensional detection and shape classification of dendritic spines from fluorescence microscopy images," *PLoS ONE*, vol. 3, no. 4, p. e1997, 2008.

[11] S. Hadjidemetriou, J. S. Duncan, D. Toomre, and D. Tuck, "Automatic quantification of microtubule dynamics," in *Proc. IEEE Int. Symp. Biomed. Imag.*, Apr. 15–18, 2004, pp. 656–659.

[12] S. Hadjidemetriou, D. Toomre, and J. S. Duncan, "Segmentation and 3d reconstruction of microtubules in total internal reflection fluorescence microscopy (TIRFM)," in *Proc. Med. Image Comput. Comput.-Assist. Interv.*, Oct. 26–30, 2005, vol. 8, pp. 761–769.

[13] A. Altinok, E. Kiris, A. J. Peck, S. C. Feinstein, L. Wilson, B. S. Manjunath, and K. Rose, "Model based dynamics analysis in live cell microtubule images," *BMC Cell Biol.*, vol. 8, p. S4, Jul. 2007.

[14] N. Cerneaz and M. Brady, "Finding curvilinear structures in mammograms," in *Proc. Int. Conf. Comput. Vis., Virtual Reality Robot. Med.*, Apr. 3–6, 1995, vol. 905, pp. 372–382.

[15] R. Zwiggelaar, T. Parr, J. Schumm, I. Hutt, C. Taylor, S. Astley, and C. Boggis, "Model-based detection of spiculated lesions in mammograms," *Med. Image Anal.*, vol. 3, no. 1, pp. 39–62, Mar. 1999.

[16] L. Wai, M. Mellor, and M. Brady, "A multi-resolution CLS detection algorithm for mammographic image analysis," in *Proc. Med. Image Comput. Comput.-Assist. Interv.*, 2004, vol. 3217, pp. 865–872.

[17] M. Barva, J. Kybic, J.-M. Mari, C. Cachard, and V. Hlavac, "Automatic localization of curvilinear object in 3D ultrasound images," *Med. Imag., Ultrason. Imag. Signal Process.*, vol. 6, no. 27, pp. 455–462, Feb. 12–17, 2005.

[18] M. Al-Rawi, M. Qutaishat, and M. Arrar, "An improved matched filter for blood vessel detection of digital retinal images," *Comput. Biol. Med.*, vol. 37, no. 2, pp. 262–267, Feb. 2007.

[19] L. Gang, O. Chutatape, and S. Krishnan, "Detection and measurement of retinal vessels in Fundus images using amplitude modified second-order Gaussian filter," *IEEE Trans. Biomed. Eng.*, vol. 49, no. 2, pp. 168–172, Feb. 2002.

[20] W. Freeman and E. Adelson, "The design and use of steerable filters," *IEEE Trans. Pattern Anal. Mach. Intell.*, vol. 13, no. 9, pp. 891–906, Sep. 1991.

[21] X. Qian, M. Brennan, D. Dione, W. Dobrucki, M. Jackowski, C. Breuer, A. Sinusas, and X. Papademetris, "A non-parametric vessel detection method for complex vascular structures," *Med. Image Anal.*, vol. 13, no. 1, pp. 49–61, Feb. 2009.

[22] H. Knutsson, "Representing local structure using tensors," in *Proc. Scand. Conf. Image Anal.*, Jun. 19–22, 1989, pp. 244–251.

[23] C. Westin, L. Wigstrom, T. Loock, L. Sjoqvist, R. Kikinis, and H. Knutsson, "Three-dimensional adaptive filtering in magnetic resonance angiography," *J. Magn. Reson. Imag.*, vol. 14, no. 1, pp. 63–71, Jul. 2001.

[24] R. Haralick, L. Watson, and T. Laffey, "The topographic primal sketch," *Int. J. Robot. Res.*, vol. 2, no. 1, pp. 50–72, Mar. 1983.

[25] L. Wang and T. Pavlidis, "Direct gray-scale extraction of features for character recognition," *IEEE Trans. Pattern Anal. Mach. Intell.*, vol. 15, no. 10, pp. 1053–1067, Oct. 1993.

[26] Y. Sato, S. Nakajima, H. Atsumi, T. Koller, G. Gerig, S. Yoshida, and R. Kikinis, "3D multi-scale line filter for segmentation and visualization of curvilinear structures in medical images," *Med. Image Anal.*, vol. 2, no. 2, pp. 143–168, Jun. 1998.

[27] K. Krissian, G. Malandain, N. Ayache, R. Vaillant, and Y. Trousset, "Model-based detection of tubular structures in 3D images," *Comput. Vis. Image Underst.*, vol. 80, no. 2, pp. 130–171, Nov. 2000.

[28] T. Koller, G. Gerig, G. Szkely, and D. Dettwiler, "Multiscale detection of curvilinear structures in 2-D and 3-D image data," in *Proc. Int. Conf. Comput. Vis.*, Jun. 20–23, 1995, pp. 864–869.

[29] T. Lindeberg, "Edge detection and ridge detection with automatic scale selection," *Int. J. Comput. Vis.*, vol. 30, no. 2, pp. 117–156, Nov. 1998.

[30] O. Tankyevych, H. Talbot, and P. Dokladal, "Curvilinear morpho-Hessian filter," in *Proc. IEEE Int. Symp. Biomed. Imag.*, May 14–17, 2008, pp. 1011–1014.

[31] D. Boukerroui, J. Noble, and M. Brady, "On the choice of band-pass quadrature filters," *J. Math. Imag. Vis.*, vol. 21, no. 1, pp. 53–80, Jul. 2004.

[32] D. Gabor, "Theory of communication," *J. Inst. Elect. Eng.*, vol. 93, pp. 429–457, 1946.

[33] D. Field, "Relations between the statistics of natural images and the response properties of cortical cells," *J. Opt. Soc. Amer.*, vol. 4, no. 12, pp. 2379–2394, Dec. 1987.

[34] M. Morrone, J. Ross, D. Burr, and R. Owens, "Mach bands are phase dependent," *Nature*, vol. 324, no. 6094, pp. 250–253, 1986.

[35] M. Morrone and R. Owens, "Feature detection from local energy," *Pattern Recognit. Lett.*, vol. 6, no. 5, pp. 303–313, Dec. 1987.

[36] M. Felsberg and G. Sommer, "The monogenic scale-space: A unifying approach to phase-based image processing in scale-space," *J. Math. Imag. Vis.*, vol. 21, no. 1, pp. 5–26, Jul. 2004.

[37] P. Kovesi, "Image features from phase congruency," *Videre, J. Comput. Vis. Res.*, vol. 1, no. 3, pp. 1–26, 2000.

[38] P. Kovesi, "Phase congruency: A low-level image invariant," *Psychol. Res.*, vol. 64, no. 2, pp. 136–148, 2000.

[39] P. Kovesi, "Phase congruency detects corners and edges," in *Proc. Int. Conf. Digit. Image Comput., Tech. Appl.*, Dec. 2003, pp. 309–318.

[40] X. Kang, P. Cheung, W. Yau, and Y. Hu, "Extracting curvilinear features from remotely sensed images using minimum cost path techniques," in *Proc. IEEE Int. Conf. Image Process.*, Sep. 26–29, 2010, pp. 1621–1624.

[41] Y. Jiang, A. Bainbridge-Smith, and A. Morris, "Blood vessel tracking in retinal images," in *Proc. Image Vis. Comput.*, Dec. 2007, pp. 126–131.

[42] A. Can, H. Shen, J. N. Turner, H. L. Tanenbaum, and B. Roysam, "Rapid automated tracing and feature extraction from retinal fundus images using direct exploratory algorithms," *IEEE Trans. Inf. Technol. Biomed.*, vol. 3, no. 2, pp. 125–138, Jun. 1999.

[43] K. Al-Kofahi, A. Can, S. Lasek, D. Szarowski, N. Dowell-Mesfin, W. Shain, J. N. Turner, and B. Roysam, "Median-based robust algorithms for tracing neurons from noisy confocal microscope images," *IEEE Trans. Inf. Technol. Biomed.*, vol. 7, no. 4, pp. 302–317, Dec. 2003.

[44] E. Dijkstra, "A note on two problems in connexion with graphs," *Numer. Math.*, vol. 1, no. 1, pp. 269–271, Dec. 1959.

[45] A. Falcao, J. Udupa, S. Samarasekera, S. Sharma, B. Hirsch, and R. Lotufo, "User-steered image segmentation paradigms: Live wire and live lane," *Graph. Models Image Process.*, vol. 60, no. 4, pp. 233–260, Jul. 1998.

[46] M. Dobie and P. Lewis, "Extracting curvilinear features from remotely sensed images using minimum cost path techniques," in *Proc. IEEE Int. Conf. Image Process.*, Nov. 13–16, 1994, vol. 3, pp. 231–235.

[47] M. Carlotto, "Enhancement of low-contrast curvilinear features in imagery," *IEEE Trans. Image Process.*, vol. 16, no. 1, pp. 221–228, Jan. 2007.

[48] K. Poon, G. Hamarneh, and R. Abugharbieh, "Live-vessel: Extending livewire for simultaneous extraction of optimal medial and boundary paths in vascular images," *Med. Image Comput. Comput.-Assist. Interv.*, vol. 10, no. 2, pp. 444–451, 2007.

[49] B. Obara, M. Fricker, and V. Grau, "Coherence enhancing diffusion filtering based on the Phase Congruency Tensor," in *Proc. IEEE International Symposium on Biomedical Imaging*, Barcelona, Spain, May 2–5, 2012.

[50] GIMP—The GNU Image Manipulation Program [Online]. Available: http://www.gimp.org/

[51] L. Boddy, J. Hynes, D. P. Bebber, and M. Fricker, "Saprotrophic cord systems: Dispersal mechanisms in space and time," *Mycoscience*, vol. 50, no. 1, pp. 9–19, 2009.

[52] E. Gelasca, B. Obara, D. Fedorov, K. Kvilekval, and B. Manjunath, "A biosegmentation benchmark for evaluation of bioimage analysis methods," *BMC Bioinformat.*, vol. 10, no. 1, p. 368, Nov. 2009.

[53] A. Hoover, V. Kouznetsova, and M. Goldbaum, "Locating blood vessels in retinal images by piecewise threshold probing of a matched filter response," *IEEE Trans. Med. Imag.*, vol. 19, no. 3, pp. 203–210, Mar. 2000.

[54] B. Obara, M. Fricker, and V. Grau, "Contrast independent detection of branching points in network-like structures," in *Proc. SPIE Med. Imag.*, San Diego, CA, Feb. 4–9, 2012.

[55] J.H. Moltz, I. Stuke, and T. Aach, "Histogram-based orientation analysis for junctions," in *Proc. Eur. Signal Process. Conf.*, Sep. 4–8, 2006, pp. 1–4.

[56] F. Faas and L. van Vliet, "Junction detection and multi-orientation analysis using streamlines," in *Proc. Comput. Anal. Images Patterns*, Aug. 27–29, 2007, vol. 4673, pp. 718–725.

Boguslaw Obara (S'02–M'10) received the M.Sc. degree in physic from the Jagiellonian University, Krakow, Poland, in 2001, and the Ph.D. degree in computer science from the Akademia Górniczo-Hutnicza University of Science and Technology, Krakow, Poland, in 2007.

He has been a Researcher with the Polish Academy of Sciences from 2001 to 2007, a Fulbright Fellow from 2006 to 2007, and a Postdoctoral Researcher from 2007 to 2009 with the University of California, Santa Barbara. He is currently a Postdoctoral Research Assistant with the University of Oxford, Oxford, U.K. His interdisciplinary research focuses on advancing the state of the art in bioimage informatics technologies aimed at a better understanding of the complex biological processes, from nano to macro.

Mark Fricker received the B.A. degree in botany from the University of Oxford, Oxford, U.K, in 1984, and the Ph.D. degree from the University of Stirling, Stirling, U.K., in 1987.

Since 1989, he has been on to a lectureship with the University of Oxford. His research interests are focused on imaging signaling and transport in complex systems using confocal ratio imaging on a microscale, scintillation imaging to map radiolabel dynamics at an intermediate scale, and network analysis and modeling to predict behavior at a macroscale.

David Gavaghan received the undergraduate degree in mathematics from Durham University, Durham, U.K., in 1986, the M.Sc. degree in numerical analysis and mathematical modeling from the University of Oxford, Oxford, U.K., in 1987, and a D.Phil. in the development of parallel numerical algorithms in 1991.

Since then, he has been working in the field of mathematical and computational modeling and has developed and now heads the Computational Biology Group, which is based in the Department of Computer Science, University of Oxford.

Vicente Grau (M'08) received the M.Eng. and Ph.D. degrees in telecommunication engineering from the Universidad Politecnica de Valencia, Valencia, Spain, in 1994 and 2001, respectively.

After research fellowships with Brigham and Women's Hospital, Boston, and Louisiana State University Health Sciences Center in New Orleans, since 2004, he has been with the University of Oxford, Oxford, U.K., where he is currently a Research Councils U.K. Academic Fellow in Computational Imaging with the Institute of Biomedical Engineering, Department of Engineering Science, and the Oxford e-Research Centre. His research interests are in biomedical image analysis and particularly in the combined use of imaging and computational models in biomedicine.